Calibration-free quantitative analysis of thin-film oxide layers in semiconductors using laser induced breakdown spectroscopy (LIBS)†

Seyyed Ali Davari,[ac] Sheng Hu,[bc] Ravi Pamu[ac] and Dibyendu Mukherjee ⓘD *[ac]

The current largest market share and continually growing industry of the semiconductor manufacturing sector in the US demands rapid and cost-effective quality control and characterization of thin film semiconducting materials. To this end, we demonstrate Laser Induced Breakdown Spectroscopy (LIBS) as a facile and effective analytical tool for rapid process-line characterization of metal-oxide-semiconductor (MOS) transistors and capacitors. Specifically, we carry out quantitative LIBS analysis on silicon oxide (SiO_2) thin-films of various thicknesses grown by high-temperature moisture-free oxidation on industrial-grade Si wafers. The stoichiometric ratios of oxygen to silicon ([O]/[Si]) in various SiO_2 films are measured by LIBS analyses using an internal calibration technique. The results are verified against benchmark analyses based on oxide layer thicknesses and laser-induced crater profile topographies from ellipsometry, scanning electron microscopy (SEM), atomic force microscopy (AFM), and profilometry measurements. The stoichiometric ratios of [O]/[Si] calculated from thickness and profilometry measurements are used to compare with our direct LIBS measurements. Our results indicate good agreement between the LIBS and profilometry calculation results, demonstrating the future capability of LIBS for thin film characterization during their industrial processing.

1. Introduction

The global energy demands in recent decades have led to significant manufacturing of semiconducting materials for solar cell applications. The efficiency and performance of solar cells strongly depend on the quality and characteristic properties of cost-effective semiconducting materials. The estimated global market share of the US in semiconductor sales is approximated at ∼50% with the most well-known materials of interest being silicon (Si) and heterojunction materials such as gallium arsenide (GaAs) and copper indium gallium diselenide (CIGS).[2] Specifically, for multi-junction solar cells, the primary parameter that affects the efficiency of thin film semiconductors such as CIGS [$CuIn_{1-x}Ga_xSe_2$] is the chemical composition of the absorber layer that determines the charge density and transport properties.[3–5] Variations in the stoichiometric ratios of the main constituents change both the structural and electronic properties of these materials.[3–5] Typically, in

the photovoltaic grade, Si impurities such as boron and oxygen change the electrical and mechanical properties significantly.[6,7] While oxygen contents can decrease the hardness of the Si wafers, a certain amount of interstitial oxygen plays a critical role in the internal gettering process.[8,9] On the other hand, the efficiency of metal-oxide-semiconductor field-effect transistors (MOSFETs) is largely driven by the properties and reliability of the SiO_2 layer,[10–12] wherein the main gate current leakage gets affected by the SiO_2 thickness.[13]

To this end, various techniques such as secondary ion mass spectrometry (SIMS),[14] X-ray fluorescence (XRF),[15] and inductively coupled plasma optical emission spectroscopy (ICP-OES)[16] have been used for the elemental analysis of thin-film semiconductor materials. Both SIMS and ICP-OES require extensive sample preparations and standards with ICP-OES specifically requiring the use of strong and harmful acids such as hydrofluoric acid. Such requirements make them destructive methods[17] that cannot be employed for *in situ* characterization during most industrial manufacturing processes. But these methods are largely relied upon for post-processing off-line quality control in industrial semiconductor sectors due to their ability to provide accurate measurements. On the other hand, only XRF can be operated under atmospheric conditions with minimal sample preparations.[18] However, XRF is not accurate for light element measurements.[19] To this end, Fourier transform infrared (FTIR) spectrometry is commonly adopted as the industrial standard technique for oxygen concentration

*a*Department of Mechanical, Aerospace, & Biomedical Engineering, University of Tennessee, Knoxville, TN 37996, USA. E-mail: dmukherj@utk.edu; Tel: +1-865-974-5309

*b*Department of Chemical & Biomolecular Engineering, University of Tennessee, Knoxville, TN 37996, USA

*c*Nano-BioMaterials Laboratory for Energy, Energetics & Environment (nbml-E³), University of Tennessee, Knoxville, TN 37996, USA

† Electronic supplementary information (ESI) available. See DOI: 10.1039/c7ja00083a

measurements in single crystalline Si wafers.[20,21] However, it suffers from interference from free carrier absorption present in heavily doped substrates.[22] To overcome such issues, the semiconductor industry currently resorts to gas fusion analysis (GFA) to measure oxygen concentrations in heavily doped epitaxial substrates. But, GFA is a highly destructive technique that has increasingly proven to be energy expensive and time consuming for the semiconductor manufacturing sector. In turn, such techniques fail to get implemented as a rapid and on-line quantitative analysis tool for quality control purposes. Specifically, for MOS devices, the challenge rests on the accurate monitoring and tailoring of thin oxide layers on silicon or other semiconducting materials to tune the inversion layer charge accumulation, mobility and transport.[23,24] Typical commercial-grade MOSFETs have been classically fabricated and extensively analyzed for gate oxide layers ranging between ∼3 nm and 20–50 nm thicknesses approximately.[23,25] To this end, the effect of gate oxide layer thicknesses on the charge mobility and capacitance in Si/SiO_2 systems becomes a critical parameter in the design of MOSFETs and has been investigated in great detail over the years.[26] In light of the aforementioned challenges in the physical and chemical characterizations of thin films for semiconductor manufacturing sectors, there exits an acute need for a robust and efficient analytical technique that can accurately monitor and measure gate oxide film characteristics during the manufacturing and processing of metal/metal oxide semiconductor materials in order to tailor their wafer electronic properties for specific device fabrication requirements.

Laser Induced Breakdown Spectroscopy (LIBS) is a relatively non-destructive spectrochemical characterization technique that can address the aforementioned issues in a facile, rapid and yet effective manner. Being a non-contact technique that is not limited by the type or physical state of the analyte materials, LIBS provides advantages that are specifically attractive for large-scale manufacturing sectors. Furthermore, it is cost-effective and capable of carrying out rapid multi-elemental analysis in one shot without compromising on the precision that makes it well-suited for *in situ* implementation in industrial environments. In the past, LIBS has been employed for chemical analysis in highly diverse applications ranging from combustion,[27–29] environmental/bio-hazard analysis,[30–33] and intermetallic nanocatalysts[34,35] to forensics,[36] explosive detection/energetic studies,[37–40] pharmaceutical,[41] and biological/biomedical studies.[42–44]

In recent years, there has been growing interest in employing LIBS for material characterization in the semiconductor industry – specifically, in regards to its choice as the future on-line quantitative analysis tool. To this end, Owens et al.[45] showed that LIBS can effectively measure heavy metal dopants in thin films. Lee et al.[46] had carried out semi-quantitative LIBS analysis to obtain the elemental ratios of constituents in a thin-film CIGS absorption layer. Added to this, Darwiche et al.[17] had extended the technique to quantify the extent of boron dopants in solar grade Si wafers using standard calibration curves. More recent efforts by Axente et al.[47] and Popescu et al.[48] have demonstrated the application of LIBS for the characterization of indium zinc oxide thin films, while Banerjee et al.[49] had

employed the technique for multi-layered profiling of organic photovoltaic coatings. Specifically, the work by Axente et al. had compared recorded spectra with spectra computed based on local thermodynamics equilibrium to obtain the atomic fraction of indium quantitatively. On the other hand, the work by Banerjee et al. had qualitatively shown that LIBS can be employed as a feedback control system during real-time laser scribing processes. It needs to be mentioned here that the calibration-free LIBS techniques proposed by Popescu et al. and Axente et al. resorted to computational models in deducing quantitative elemental fractions, as compared to a methodology based on raw spectral data collected from analyte samples as developed in our previous studies and implemented in the current study. Additionally, while the average thin films used in these studies were about 350 nm (Popescu et al.[48]) and 500 nm (Axente et al.[47]) thick, they did not attempt to report the lowest film thickness analytically detectable by LIBS.

In our efforts to investigate the feasibility of LIBS as the future analytical tool for rapid quantitative characterization of industrial grade thin film MOSs, this study presents a calibration-free LIBS technique for quantifying thin-film oxide layers grown atop industrial-grade Si wafers. Commercial Si wafers obtained were treated at different temperatures in order to synthesize and control the oxide layer thicknesses systematically. The ratio of ablated oxygen (O) to Si is measured based on the O and Si atomic emission signals by using the LIBS internal calibration technique developed in our earlier studies.[32,34,40] The oxide layer thicknesses along with the crater sizes and profiles are measured using ellipsometry, scanning electron microscopy (SEM), atomic force microscopy (AFM), and optical profilometry. Based on the profilometry measurements, the ratios of O to Si in the oxide layers and their film thicknesses on the Si wafers are estimated, and compared to the LIBS results.

2. Experimental details

2.1 LIBS set-up

The experimental set-up is illustrated in Fig. 1. The laser-induced plasma is generated on the sample target surface using a Q-switched Nd-YAG laser of nominal wavelength 1064 nm operating at 10 Hz repetition rates, 200 mJ per pulse energy, and a pulse width of 8 ns (Make: Insight Model: 122551-R). The laser is focused with a 25 mm diameter fused silica lens (focal length = 35 mm) at the focal point on the target surface (Fig. 1). The spot size on the sample is set to 75 μm diameter, which creates a plasma volume of ∼1–2 mm^3 approximately. Since the oxide layer is thin, only one laser shot per spot is collected. To improve the statistical average of the signal intensity for each analyte of interest, spectral data over approximately 100–150 spots are collected.

The plasma emission is collected with a fiber optic port carrying a pair of collimation-focusing lenses mounted at a 45 degree collection angle (Fig. 1), which yields the optimum intensity from the plasma volume. The focused light is transmitted to a Czerny-Turner spectrometer (Make: Andor Technology; Model: Shamrock – SR-303i-A) with a 1200 grooves per mm grating (resolution of 0.1 nm at 500 nm) and a nominal
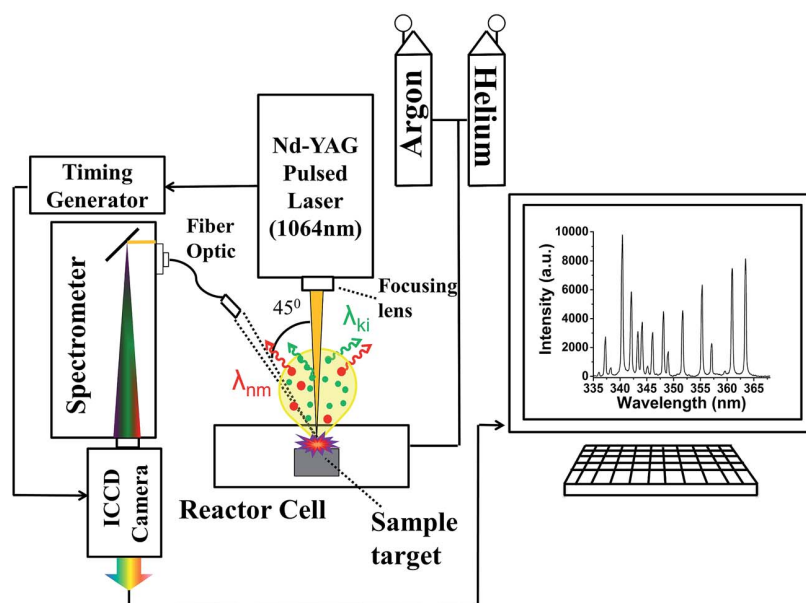
Fig. 1 Schematic of the LIBS experimental set-up used for characterizing samples.

dispersion of 2.58 nm mm^{-1}. The slit width is fixed at 95 μm for all experiments carried out here in order to have the optimum spectral line intensity and resolution. A time-gated intensified charge-coupled device (ICCD) detector array (1024 × 1024 CCD) (Make: Andor Technology; Model: DH334T-18U-E3) detects the spectral lines at the spectrometer exit focal plane. The time gating is synchronized with the laser Q-switch through an in-built timing generator in the ICCD camera set-up.

2.2 SiO$_2$ film synthesis

Commercial silicon wafers, purchased from UniversityWafer, Inc. (ID#2444), were cut into approximately 1 × 1 cm^2 pieces. The wafers underwent dry thermal oxidation in laboratory furnaces at various temperatures in order to create and control the oxide layer thickness on top of the wafer. Specifically, the wafers were baked for 20 minutes at oven temperatures ranging from 900 °C to 1000 °C with a 25 °C step, and with one final sample being baked at 1050 °C. The samples were tested using LIBS in an in-house built reactor cell while both helium (6 lpm) and argon (2 lpm) were purged into the cell as the buffer gas. The choice of flow rates is discussed in the Results and discussion (2.1). To account for any unwanted background trace oxygen that might exist in the buffer gas or the control Si wafer samples, the background emission for O I is subtracted from the emissions from the baked Si wafer samples. Here, the background is considered as the emissions from the Si wafers without any oxide layer. To accomplish that, Si wafers are dipped into 10% hydrofluoric (HF) acid for 10 minutes.

2.3 LIBS methodology

In this study, atomic emission lines were selected from the NIST Atomic Energy Levels Data Center[1] according to their relative line strength, and transition probabilities. To gain maximum

accuracy in the results, optimal gate delays are determined based on the variations of signal-to-noise ratios (SNRs) as a function of gate delays for the respective elemental species. The SNR is calculated by measuring the peak signal value at the specific wavelength of interest for a spectral line divided by the noise of the spectra. The noise is defined as the root mean square over the baseline (∼over 40 pixels) adjacent to the analyte peak. The optimum SNR is used as the effective emission (I_{em}) for the population density calculations of the respective atomic species based on the Maxwell–Boltzmann distribution:

$$I_{em} = hc \frac{A_{ki}}{\lambda_{ki}} N_i \frac{g_k}{g_i} \exp\left(-\frac{\Delta E_{ki}}{k_B T_{exc}} \right) \quad (1)$$

where N_i, A_{ki}, λ_{ki}, g_k, and g_i are the atomic number densities at the lower energy state, Einstein's transition probability, emitted wavelength, and statistical weights for the higher (k) and lower (i) energy states, respectively, for the specific atomic transition of interest. ΔE_{ki} is the energy difference between the k and i states, and T_{exc} is the plasma excitation temperature at the optimal gate delays. Boltzmann and Planck's constant are indicated by k_B (1.38064 × 10^{-23} m^2 kg s^{-2} K^{-1}) and h (6.62607 × 10^{-34} m^2 kg s^{-1}), respectively, and c (3 × 10^8 m s^{-1}) is the speed of light in vacuum.

The plasma excitation temperatures (T_{exc} and K) are determined from the slope of the fit to the linear Boltzmann plot of $\ln(I_{em}\lambda_{ki}/g_k A_{ki})$ as a function of normalized upper energy levels (E_k/k_B) (derived from eqn (1)) for multiple strong lines with sufficiently widespread upper energy levels. It is worth mentioning that the Boltzmann distribution (eqn (1)) is valid under the assumption of local thermodynamic equilibrium (LTE) conditions for the laser-induced plasma. The conditions are established when the plasma quenching processes are predominantly collisional rather than radiative. Typically, such

conditions are observed within longer times of plasma evolution (>1 μs).[34,40,50] Thus, all our LIBS emission lines are collected at gate delays beyond 1 μs. Finally, the population densities of the analyte species of interest and bulk matrix or background species are calculated under similar plasma conditions. As discussed in detail in our earlier studies,[34,40] any artifacts arising from the optical/experimental set-up or time dependent plasma characteristics is nullified through the use of the internal calibration technique. Based on this technique, the stoichiometric ratios between any two species X and Y of interest is estimated as

$$R = \frac{[\mathrm{X}]}{[\mathrm{Y}]} = \frac{\left[N_i^{\mathrm{X\,I}}/N_i^{\mathrm{B\,I}}\right]_{@\mathrm{GD}=t_1}}{\left[N_i^{\mathrm{Y\,I}}/N_i^{\mathrm{B\,I}}\right]_{@\mathrm{GD}=t_2}} \quad (2)$$

where N_i^{X}, and N_i^{B} represent the lower energy state population densities of the analyte X, and the bulk background (matrix) species, respectively. The aforementioned normalization of population densities of the desired analyte species is carried out at the optimal gate delays (GDs) for the LIBS emissions of the respective species.

2.4 Crater characterization

Prior to sample ablations for the LIBS measurements, the oxide layer thicknesses on the respective heat-treated Si wafer samples are measured using an ellipsometer (Horiba Sci.; Model: UVISEL). Subsequent to the LIBS measurements, the sample crater sizes are also measured using a profilometer (Veeco Wyko Non-contact Profilometer NT3300). Finally, we use atomic-force microscopy (AFM; Make: NT-MDT; Model: NTEGRA Spectra) in the tapping mode with silicon cantilever tips (Model: AppNano Model: ACTA) and scanning electron microscopy (SEM) in order to verify the crater sizes and profiles further.

3. Results and discussion

3.1 Optimizing measurements and plasma parameters

In this study, atomic transition lines were chosen from the NIST Atomic Energy Levels Data Center.[1] For detailed quantitative LIBS analyses, the atomic emission lines of O I (777.19 nm) and Si I (288.16 nm) were selected. The specific choice of these lines was based on their robust transition probabilities and line strengths. To this end, Table 1 reports the detailed spectral data for the aforementioned emission lines of choice. Fig. 2a and b show the spectral emissions of O I (777.19 nm) and Si I (288.16 nm) lines, respectively. It is observed in Fig. 2a that in the presence of 6 lpm helium mixed with 2 lpm argon, the O I
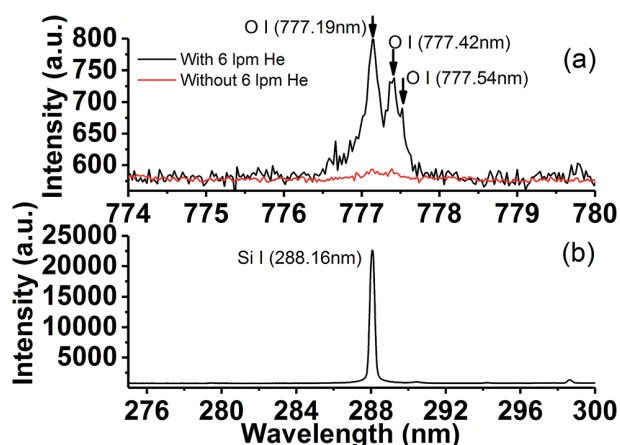

Fig. 2 Spectral emission signature for (a) O I (777.19 nm) with and without helium in the buffer gas, and (b) Si I (288.16 nm) lines at the respective gate delays of 3.5 μs, and 5 μs.

(777.19 nm) signal enhances significantly. Such observations were also previously reported in the work of Mukherjee et al.[40] where it was discussed that the addition of helium creates a less dense plasma that effectively reduces the background continuum noise. However, reducing plasma density eventually deteriorates the emission signals too. Therefore, based on the specific sample of study, an optimal value for the ratio of helium to argon flow rates provides ideal signal enhancements. To this end, the O I (777.19 nm) SNR is plotted as a function of He/Ar flow rate ratio as the background buffer gas (Fig. 3). It is clearly observed that an optimal ratio of ~3 for the He/Ar ratio in the background buffer gas produces the maximum O I SNR of ~18. For lower ratios, the plasma is relatively thick that subdues the signal enhancement while for greater ratios, the plasma becomes too thin and the O I (777.19 nm) emission signal is decreased. Hence, for the rest of the experiments, a mixture of 2 lpm of argon and 6 lpm of helium was used as the buffer gas. Furthermore, in order to gain the maximum accuracy for the population density calculations from the LIBS signals, the optimal gate delays for each of the Si I and O I emission lines are determined by plotting their respective SNRs as a function of gate delays. Fig. 4a and b show the temporal evolution of O I (777.19 nm) and Si I (288.16 nm) emission lines, respectively, at the gate width of 2 μs. From these plots, the optimal gate delays are estimated to be 3.5 μs and 5 μs for the O I and Si I emission lines, respectively. Based on the linear parts of Fig. 4c and d the gate width of 14 μs is used for both O I and Si I.

Table 1 Atomic spectral database[1] for Si I and O I emission lines used for the population density calculations during quantitative analysis of ablated spots

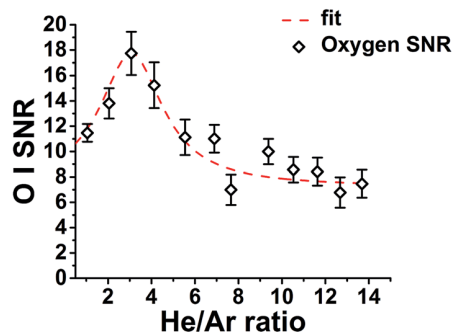| Species	Wavelength, λ_{ki} (nm)	Transition probability, A_{ki} (10^6 s^{-1})	Upper energy level, E_k (eV)	Lower energy level, E_i (eV)	g_k	g_i
Si I	288.16	218	5.082	0.781	3	5
O I	777.19	36.9	10.741	9.146	7	5

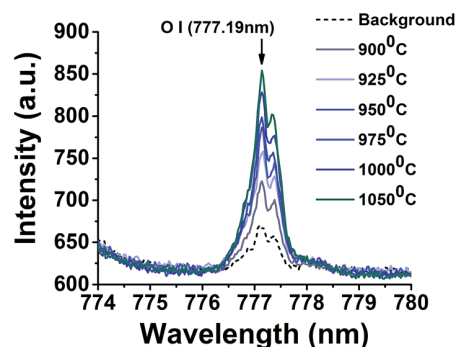Fig. 3 Optimizing oxygen SNR with respect to the ratio of helium to argon flow rates.

Fig. 5 Spectral emission signature of O I (777.19 nm) for samples with various oxide layer thicknesses.

3.2 LIBS measurements

Fig. 5 shows the characteristic emission spectra of O I (777.19 nm) acquired from the control (devoid of the oxide layer) and specific samples baked at different temperatures. It can be observed from Fig. 5 that the control sample still shows some background emission at 777.19 nm, which is associated with the ubiquitous oxygen contents in the reactor cell that is almost impossible to eliminate in the absence of extremely high-end vacuum systems. However, the specific heated samples show distinct enhancement of the emissions at O I (777.19 nm) as compared to the background emission which allows for back-ground subtractions. Moreover, the O I (777.19 nm) emissions increase systematically as the oxide layers of the specific samples increase due to their baking at increasing

temperatures. This increasing oxide layer thickness is also confirmed by ellipsometry measurements in the next section. The plasma excitation temperatures, T_{exc}, required for the population density calculations are estimated from the linear Boltzmann plots as explained in the Experimental section earlier. Here, the linear Boltzmann plots are constructed at the two different time delays (3.5 μs and 5 μs) of the plasma evolution using a series of Ar I lines with known spectral properties as listed in Table 2. Fig. 6a and b illustrate the Boltzmann plots acquired at 3.5 μs and 5 μs gates, whose slopes indicate T_{exc} = 17 126 K and 15 166 K, respectively. Similarly, the T_{exc} values for all the different heat-treated samples are estimated and reported in Table 3. The estimated excitation temperatures are employed to calculate the relative population
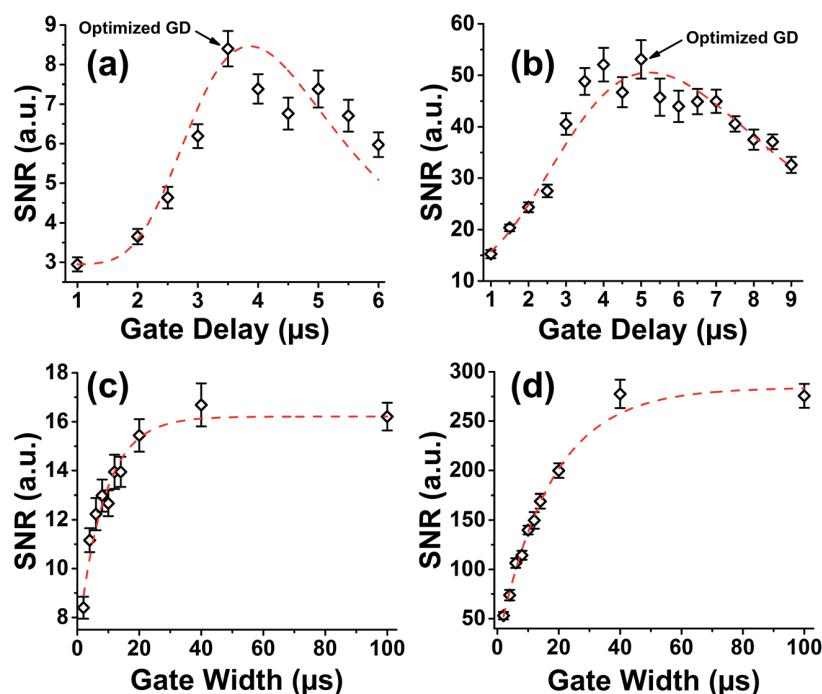

Fig. 4 Temporal evolution of the signal-to-noise ratio for (a) O I (777.19 nm),and (b) Si I (288.16 nm) over gate delays. The optimal gate delays were determined to be 3.5 μs and 5 μs for the peak signal-to-noise ratio for O I (777.19 nm) and (b) Si I (288.16 nm), respectively. (c) Temporal evolution of the signal-to-noise ratio for (c) O I (777.19 nm) and (d) Si I (288.16 nm) over the gate width.

Table 2 Atomic spectral database[1] for different Ar atomic emission lines used for the plasma excitation temperature calculations at 3.5 μs and 5 μs for spectral analysis of ablated spots

Species	Wavelength, λ_{ki} (nm)	Transition probability, A_{ki} (10^6 s^{-1})	Upper energy level, E_k (eV)	Lower energy level, E_i (eV)	g_k	g_i
Ar I	415.859	1.40	14.528	11.548	5	5
Ar I	420.068	0.967	14.499	11.548	7	5
Ar I	425.936	3.98	14.738	11.828	1	3
Ar I	427.217	0.797	14.525	11.624	3	3
Ar I	433.356	0.568	14.688	11.828	5	3
Ar I	696.543	6.39	13.328	11.548	3	5
Ar I	706.722	3.80	13.302	11.548	5	5
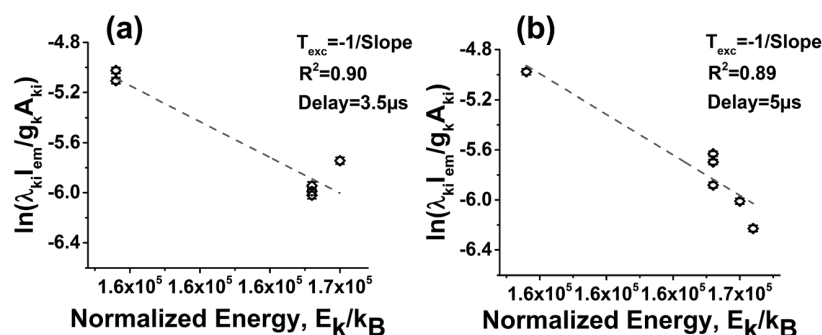
Fig. 6 The linear Boltzmann plots generated from Ar I lines listed in Table 2, and used for T_{exc} calculations at the respective gate delays of 3.5 μs and 5 μs.

Table 3 [O]/[Si] ratios for various samples and respective plasma excitation temperatures at 3.5 μs and 5 μs

Sample treated temperature	[O]/[Si] (ablation-cylinder)	[O]/[Si] (LIBS)	[O]/[Si] (ablation-cone frustum)	Plasma excitation temp. T_{exc} (K)	
				at 3.5 μs	at 5 μs
900 °C	0.022	0.025	0.046	17 125 ± 3833	15 166 ± 2893
925 °C	0.027	0.047	0.047	17 803 ± 3706	15 849 ± 3235
950 °C	0.032	0.045	0.079	17 372 ± 2898	16 427 ± 3637
975 °C	0.051	0.052	0.102	20 802 ± 4162	17 580 ± 4550
1000 °C	0.057	0.098	0.133	21 535 ± 4692	20 311 ± 5826
1050 °C	0.078	0.097	0.179	20 142 ± 4620	18 255 ± 4628

densities of oxygen ($N_i^{O\ I}$), silicon ($N_i^{Si\ I}$) and argon ($N_i^{Ar\ I}$) from the respective atomic emission lines of O I (777.19 nm), Si I (288.16 nm) and Ar I (series of lines indicated in Table 2). Using Ar as the bulk species in the plasma for the normalization shown in eqn (2), the ratio of oxygen to silicon ([O]/[Si]) is calculated as

$$R = \frac{[O]}{[Si]} = \frac{\left[N_i^{O\ I\ (777.19\ nm)} \middle/ N_i^{Ar\ I} \right]_{@GD=3.5\ \mu s}}{\left[N_i^{Si\ I\ (288.16\ nm)} \middle/ N_i^{Ar\ I} \right]_{@GD=5\ \mu s}} \quad (3)$$

The results for [O]/[Si] (LIBS) ratios are tabulated in Table 3. In order to compare the results obtained from the quantitative LIBS analyses, the amounts of ablated materials are also estimated by characterizing the oxide layer thicknesses and crater profile using ellipsometry, SEM, AFM and profilometry

measurements. Based on the profilometry calculation, discussed in the following sections, the amount of ablated oxygen and silicon is estimated, and used for calculating [O]/[Si] (ablation) ratios in Table 3 from the crater ablation analyses that will be presented in the following sections.

3.3 Oxide layer thickness measurements

As the first step toward characterization of the amount of elemental species in the laser ablated crater from the LIBS measurements, the initial oxide layer thicknesses from the samples are measured using ellipsometry. A classical dispersion model based on SiO$_2$ on top of a silicon substrate is used for curve fitting, and observed that the model and the acquired data are in excellent agreement as shown in Fig. S1 in the ESI.† For each oxidation temperature, four different pieces and on each piece four different spots are analyzed for the ellipsometry

Table 4 The oxide layer thicknesses for various oxidation temperatures obtained by ellipsometry measurements

Sample treated temperature	900 °C	925 °C	950 °C	975 °C	1000 °C	1050 °C
Thickness (nm)	50.94 ± 0.25	64.63 ± 0.19	75.62 ± 0.05	122.10 ± 0.01	136.93 ± 0.35	188.82 ± 0.37

measurements. The oxide layer thicknesses are reported in Table 4. As expected, the oxide layer thickness grows further as the oxidation temperature increases. Moreover, the small standard deviations indicate that the oxide layer is uniform across the sample surface.

3.4 Crater measurements

Fig. 7 shows the SEM image of the crater obtained from the ablation of a representative sample (Si wafer baked at 950 °C). The image indicates that the ablation spot diameter is approximately 200 μm, while the crater depth can be qualitatively observed to be shallow. In order to obtain the crater depth quantitatively, the samples are measured using a profilometer (Fig. 8a). The profilometry result also indicates that the ablation spot diameter is 200 μm, while the crater depth is approximated to be ~2.5 μm. For a secondary verification of the crater depth, the ablation spots are also topographically imaged using AFM in tapping mode with a slow scan rate. Due to the AFM instrument limitations, only a 100 μm × 100 μm window can be measured. Hence, the measured window was chosen such that it spanned over ~30 μm of the spot edge and ~70 μm of the crater. As seen from the z-profile of the AFM topography image for the selected window in Fig. 8b, the crater depth can be confirmed to be ~2.5 as also corroborated from our profilometry measurements.

3.5 LIBS and profile calculation comparison

Based on the oxide layer thickness, the ablation spot diameter and the crater depth, two simple geometric models, namely cylindrical and a frustum of a cone, are constructed to calculate the amount of ablated O and Si, and the ablated [O]/[Si] ratio was calculated as depicted in Fig. 9a and b. Based on these geometries for the ablated volume, the [O]/[Si] ratio can be determined as

$$\frac{[O]}{[Si]} = \frac{2\left(\frac{\rho_{SiO_2}}{M_{w,SiO_2}}\right) V_{SiO_2}}{\left(\frac{\rho_{SiO_2}}{M_{w,SiO_2}}\right) V_{SiO_2} + \left(\frac{\rho_{Si}}{M_{w,Si}}\right) V_{Si}} \tag{4}$$

where V_{SiO_2} and V_{Si} are the ablated volumes of the oxide layer and silicon substrate, respectively, which can be expressed by the oxide layer thickness (δ_{SiO_2}), and crater depth (h). M_w and ρ are the molecular weights and densities, respectively, and are tabulated in Table 5 for Si and SiO₂. Fig. 10 illustrates the results for the ratio of [O]/[Si] as obtained from LIBS plotted as a function of the respective ratios obtained from the crater profile or ablation characterizations based on the assumption of cylindrical and cone frustum geometries. The red and the blue dotted line represent the linear fits to the calculated values for the cylindrical and the cone-frustum geometry, respectively. It can be observed that the LIBS results are relatively in good agreement and indicate a linear correlation with the profilometry calculations. The error bars are calculated based on the error propagation for both
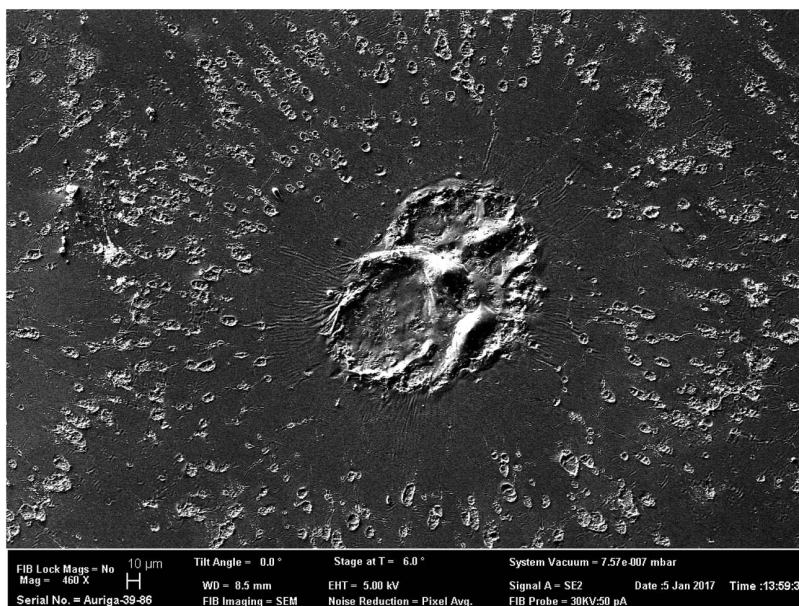

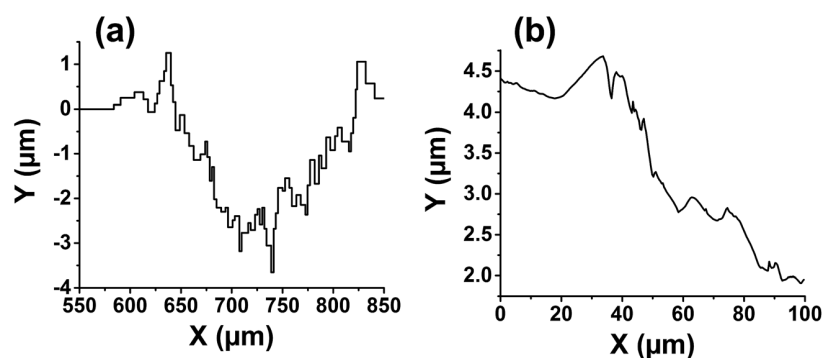**Fig. 7** SEM image of the ablated spots used for measuring the ablated spot diameter.

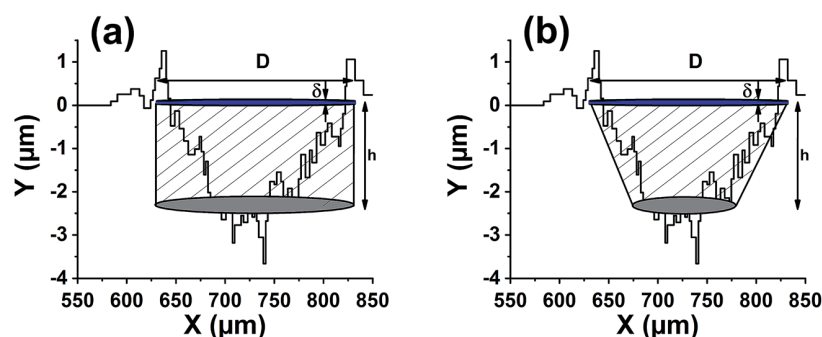**Fig. 8** Depth profile measurement for the ablated spots using (a) optical profilometry and (b) AFM.

Fig. 9 The simple geometric models: (a) cylinder and (b) cone–frustum showing ablation volume used for calculating the [O]/[Si] ratio.

Table 5 Si and SiO$_2$ properties used for calculating the [O]/[Si] ratio from the profilometric model

Properties	Molecular weight, M_w (g mol^{-1})	Density, ρ (g cm^{-3})
SiO$_2$	60.083	2.65
Si	28.085	2.33

methods due to uncertainties in plasma temperature, shot-to-shot variation in laser-induced plasma, and standard deviations in crater measurements. The deviations from the profilometry calculations can be related to the errors in measuring crater profiles and simplistic geometric models, which change the amount of ablated silicon. Analyzing the crater profile of the ablation spot indicates that the amount of ablated silicon based on the cylindrical geometry is greater than that of the actual ablated silicon, while the cone-frustum underestimates the amount of ablated silicon. In fact, the ideal one-to-one linear correlation between the [O]/[Si] ratios from the LIBS measurements and the profilometry analyses appears to lie within the two sets of data for the cylindrical and the cone-frustum profile geometry case (*i.e.* the red and the blue dotted linear fit). Furthermore, the errors bars of the [O]/[Si] ratios from the LIBS measurements commensurate with the spread in the data for the aforementioned two cases thereby indicating that the deviations are within the experimental margins of error. Finally, we present

the LIBS calibration for the quantitative determination of thin-film oxide layer thickness on Si wafer by plotting the O I subtracted signal as a function of oxide layer thicknesses (from ellipsometry measurements) in Fig. 11. Based on the slope of the calibration curve, the minimum distinguishable oxide layer (δ_{min}) that can be estimated from our current LIBS set-up is found to be

$$\delta_{min} = \frac{3\sigma_B}{S} \quad (5)$$

where σ_B is the standard deviation of the background and S is the slope of the calibration curve. This gives the estimated thinnest detectable oxide layer using LIBS as $\delta_{min} \sim 10.51 \pm 1.44$ nm.
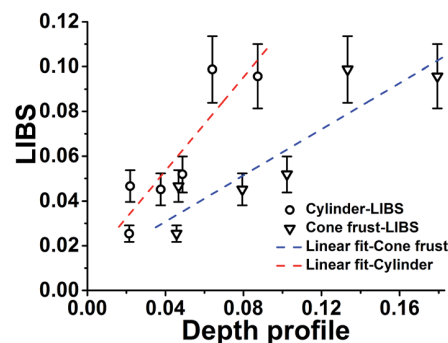

Fig. 10 Comparison between the [O]/[Si] ratio directly measured by LIBS and calculated by characterizing the ablated spot.
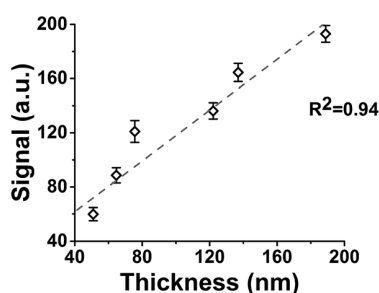
Fig. 11 Calibration curve of the O I (777.19 nm) SNR as a function of oxide layer thickness.

4. Conclusion

We have employed LIBS for calibration-free quantitative analysis of thin-film silicon dioxide layers with various thicknesses synthesized *via* dry thermal oxidation of Si wafers. To this end, an internal calibration technique was applied that involved effective normalization of the analyte species densities by bulk species densities in the laser-induced plasma. The species densities of O (analyte) and Si (bulk) for the SiO_2 films in this case were estimated from the respective atomic emission lines under identical plasma conditions to generate the ablated oxygen to silicon ([O]/[Si]) ratio. The results from our LIBS analyses were corroborated by the [O]/[Si] ratios directly calculated from the ablated spots by measuring the oxide layer thicknesses and crater profiles using ellipsometry, SEM, AFM and profilometry techniques. The results are in good agreement with each other within the margins of experimental uncertainty. The small deviations of the LIBS results from the profilometry calculations were attributed to the errors in the depth measurements and assumed geometry of the crater profile. Based on our measurements, a calibration curve for the LIBS analysis was established which indicated the detection limit for the thinnest oxide layer thickness to be ~10.5 ± 1.4 nm. The results from the current work provide future directions towards the promising potential of LIBS as an analytical tool for rapid screening of oxide layers in MOS transistors/capacitors, and more generally, for surface composition analysis of thin-film materials.

Acknowledgements

References

1 A. Kramida, Yu. Ralchenko and J. Reader, *NIST ASD Team. NIST Atomic Spectra Database (Version 5.3)*, 2015, http://physics.nist.gov/asd.

2 U. S. GAO, *Nanomanufacturing: Emergence and Implications for U.S. Competitiveness, the Environment, and Human Health*, United States Government Accountability Office (U.S. GAO), 2014.

3 A. V. Mudryi, *et al.*, Structural and optical properties of thin films of Cu(In,Ga)Se-2 semiconductor compounds, *J. Appl. Spectrosc.*, 2010, **77**(3), 371–377.

4 S. H. Wei, S. B. Zhang and A. Zunger, Effects of Ga addition to $CuInSe_2$ on its electronic, structural, and defect properties, *Appl. Phys. Lett.*, 1998, **72**(24), 3199–3201.

5 T. Dullweber, *et al.*, Study of the effect of gallium grading in Cu(In,Ga)Se-2, *Thin Solid Films*, 2000, **361**, 478–481.

6 D. Macdonald, *et al.*, Light-induced boron-oxygen defect generation in compensated p-type Czochralski silicon, *J. Appl. Phys.*, 2009, **105**(9), 093704.

7 R. Falster and V. V. Voronkov, On the properties of the intrinsic point defects in silicon: a perspective from crystal growth and wafer processing, *Phys. Status Solidi B*, 2000, **222**(1), 219–244.

8 J. H. Chen, *et al.*, Rapid-thermal-anneal-based internal gettering for germanium-doped Czochralski silicon, *Appl. Phys. A: Mater. Sci. Process.*, 2009, **94**(4), 905–910.

9 I. G. Kim and J. S. Kwon, Reduction of grown-in defects by vacancy-assisted oxygen precipitation in high density dynamic random access memory, *Appl. Phys. Lett.*, 2003, **83**(23), 4863–4865.

10 X. Shen, S. Dhar and S. T. Pantelides, Atomic origin of high-temperature electron trapping in metal-oxide-semiconductor devices, *Appl. Phys. Lett.*, 2015, **106**(14), 143504.

11 A. Chanthaphan, *et al.*, Improved bias-temperature instability characteristics in SiC metal-oxide-semiconductor devices with aluminum oxynitride dielectrics, *Appl. Phys. Lett.*, 2014, **104**(12), 122105.

12 X. Y. Yang, B. Lee and V. Misra, High Mobility 4H-SiC Lateral MOSFETs Using Lanthanum Silicate and Atomic Layer Deposited SiO_2, *IEEE Trans. Electron Devices*, 2015, **36**(4), 312–314.

13 Y. C. Wang, *et al.*, Investigation of Leakage Current Mechanisms in La_2O_3/SiO_2/4H-SiC MOS Capacitors with Varied SiO_2 Thickness, *J. Electron. Mater.*, 2016, **45**(11), 5600–5605.

14 K. Durose, *et al.*, Physical characterization of thin-film solar cells, *Prog. Photovoltaics*, 2004, **12**(2–3), 177–217.

15 P. Jackson, *et al.*, New world record efficiency for Cu(In,Ga) Se-2 thin-film solar cells beyond 20%, *Prog. Photovoltaics*, 2011, **19**(7), 894–897.

16 S. Martinuzzi, *et al.*, n-Type Multicrystalline Silicon Wafers Prepared from Plasma Torch Refined Upgraded Metallurgical Feedstock, *Prog. Photovoltaics*, 2009, **17**(5), 297–305.

17 S. Darwiche, *et al.*, Laser-induced breakdown spectroscopy for photovoltaic silicon wafer analysis, *Prog. Photovoltaics*, 2012, **20**(4), 463–471.

18 S. H. Lee, *et al.*, Ablation and Spectroscopic Characteristics of Thin $CuIn_{1-x}Ga_xSe_2$ Solar Cell Films Fabricated by Co-Evaporation and Co-Sputtering Processes, *Int. J. Pr. Eng. Man.–G.T.*, 2014, **1**(1), 17–24.

19 A. A. Bol'shakov, *et al.*, Laser-induced breakdown spectroscopy in industrial and security applications, *Appl. Opt.*, 2010, **49**(13), C132–C142.

20 Z. X. Liu, A. Masuda and M. Kondo, Investigation on the crystal growth process of spherical Si single crystals by melting, *J. Cryst. Growth*, 2009, **311**(16), 4116–4122.

21 C. Veve, M. Stemmer and S. Martinuzzi, Oxygen precipitates in annealed CZ silicon wafers detected by SIRM and FTIR spectroscopy, *Mater. Sci. Eng., B*, 1996, **36**(1–3), 200–203.

22 D. E. Hill, Determination of Interstitial Oxygen Concentration in Low-Resistivity N-Type Silicon-Wafers by Infrared-Absorption Measurements, *J. Electrochem. Soc.*, 1990, **137**(12), 3926–3928.

23 A. Hartstein and N. F. Albert, Determination of the inversion-layer thickness from capacitance measurements of metal-oxide-semiconductor field-effect transistors with ultrathin oxide layers, *Phys. Rev. B: Condens. Matter Mater. Phys.*, 1988, **38**(2), 1235–1240.

24 C. G. Sodini, T. W. Ekstedt and J. L. Moll, Charge Accumulation and Mobility in Thin Dielectric Mos-Transistors, *Solid-State Electron.*, 1982, **25**(9), 833–841.

25 A. Toriumi, *et al.*, Experimental-Determination of Finite Inversion Layer Thickness in Thin Gate Oxide MOSFETs, *Surf. Sci.*, 1986, **170**(1–2), 363–369.

26 M. S. Liang, *et al.*, Inversion-Layer Capacitance and Mobility of Very Thin Gate-Oxide MOSFETs, *IEEE Trans. Electron Devices*, 1986, **33**(3), 409–413.

27 F. Ferioli and S. G. Buckley, Measurements of hydrocarbons using laser-induced breakdown spectroscopy, *Combust. Flame*, 2006, **144**(3), 435–447.

28 F. Ferioli, P. V. Puzinauskas and S. G. Buckley, Laser-induced breakdown spectroscopy for on-line engine equivalence ratio measurements, *Appl. Spectrosc.*, 2003, **57**(9), 1183–1189.

29 M. Ghezelbash, *et al.*, Experimental investigation of atomic and ionic titanium lines, diatomic TiO γ transition and continuum background radiation *via* magnetically confined LIBS, *Ceram. Int.*, 2017, **43**(11), 8356–8363.

30 D. A. Cremers, *et al.*, Measuring total soil carbon with laser-induced breakdown spectroscopy (LIBS), *J. Environ. Qual.*, 2001, **30**(6), 2202–2206.

31 R. Wisbrun, *et al.*, Detector for Trace Elemental Analysis of Solid Environmental-Samples by Laser-Plasma Spectroscopy, *Anal. Chem.*, 1994, **66**(18), 2964–2975.

32 D. Mukherjee and M. D. Cheng, Quantitative analysis of carbonaceous aerosols using laser-induced breakdown spectroscopy: a study on mass loading induced plasma matrix effects, *J. Anal. At. Spectrom.*, 2008, **23**(1), 119–128.

33 M. Yao, *et al.*, Detection of heavy metal Cd in polluted fresh leafy vegetables by laser-induced breakdown spectroscopy, *Appl. Opt.*, 2017, **56**(14), 4070–4075.

34 S. A. Davari, S. Hu and D. Mukherjee, Calibration-free quantitative analysis of elemental ratios in intermetallic nanoalloys and nanocomposites using Laser Induced Breakdown Spectroscopy (LIBS), *Talanta*, 2017, **164**, 330–340.

35 S. A. Davari, *et al.*, Rapid elemental composition analysis of intermetallic ternary nanoalloys using calibration-free quantitative Laser Induced Breakdown Spectroscopy (LIBS), *MRS Adv.*, 2017, 1–6.

36 B. E. Naes, *et al.*, A comparison of laser ablation inductively coupled plasma mass spectrometry, micro X-ray fluorescence spectroscopy, and laser induced breakdown spectroscopy for the discrimination of automotive glass, *Spectrochim. Acta, Part B*, 2008, **63**(10), 1145–1150.

37 J. L. Gottfried, Influence of metal substrates on the detection of explosive residues with laser-induced breakdown spectroscopy, *Appl. Opt.*, 2013, **52**(4), B10–B19.

38 F. C. De Lucia and J. L. Gottfried, Influence of Molecular Structure on the Laser-Induced Plasma Emission of the Explosive RDX and Organic Polymers, *J. Phys. Chem. A*, 2013, **117**(39), 9555–9563.

39 J. L. Gottfried, *et al.*, Laser-induced breakdown spectroscopy for detection of explosives residues: a review of recent advances, challenges, and future prospects, *Anal. Bioanal. Chem.*, 2009, **395**(2), 283–300.

40 D. Mukherjee, A. Rai and M. R. Zachariah, Quantitative laser-induced breakdown spectroscopy for aerosols *via* internal calibration: application to the oxidative coating of aluminum nanoparticles, *J. Aerosol Sci.*, 2006, **37**(6), 677–695.

41 D. Mukherjee and M. D. Cheng, Characterization of carbon-containing aerosolized drugs using laser-induced breakdown spectroscopy, *Appl. Spectrosc.*, 2008, **62**(5), 554–562.

42 K. Stepankova, *et al.*, Laser ablation methods for analysis of urinary calculi: comparison study based on calibration pellets, *Spectrochim. Acta, Part B*, 2013, **81**, 43–49.

43 J. D. Hybl, G. A. Lithgow and S. G. Buckley, Laser-induced breakdown spectroscopy detection and classification of biological aerosols, *Appl. Spectrosc.*, 2003, **57**(10), 1207–1215.

44 S. A. Davari, *et al.*, *In vitro* analysis of early calcification in aortic valvular interstitial cells using Laser-Induced Breakdown Spectroscopy (LIBS), *J. Biophotonics*, DOI: 10.1002/jbio.201600288.

45 T. Owens, *et al.*, Ultrafast thin-film laser-induced breakdown spectroscopy of doped oxides, *Appl. Opt.*, 2010, **49**(13), C67–C69.

46 S. H. Lee, *et al.*, Analysis of the absorption layer of CIGS solar cell by laser-induced breakdown spectroscopy, *Appl. Opt.*, 2012, **51**(7), B115–B120.

47 E. Axente, *et al.*, Accurate analysis of indium-zinc oxide thin films *via* laser-induced breakdown spectroscopy based on plasma modeling, *J. Anal. At. Spectrom.*, 2014, **29**(3), 553–564.

48 A. C. Popescu, *et al.*, Analysis of indium zinc oxide thin films by laser-induced breakdown spectroscopy, *J. Appl. Phys.*, 2011, **110**(8), 083116.

49 S. Banerjee, *et al.*, Characterization of organic photovoltaic devices using femtosecond laser induced breakdown spectroscopy, *Appl. Surf. Sci.*, 2016.

50 D. W. Hahn and N. Omenetto, Laser-Induced Breakdown Spectroscopy (LIBS), Part I: Review of Basic Diagnostics and Plasma–Particle Interactions: Still-Challenging Issues Within the Analytical Plasma Community, *Appl. Spectrosc.*, 2010, **64**(12), 335A–366A.